

The Consistent Multi-fluid Advection method

T. Plewa ^{*} and E. Müller

Max-Planck-Institut für Astrophysik, Karl-Schwarzschild-Straße 1, Postfach 1523, 85740 Garching b. München, Germany
e-mail: (tomek,ewald)@mpa-garching.mpg.de

Received ; accepted

Abstract. Simple modifications for higher-order Godunov-type difference schemes are presented which allow for accurate advection of multi-fluid flows in hydrodynamic simulations. The constraint that the sum of all mass fractions has to be equal to one in every computational zone throughout the simulation is fulfilled by renormalizing the mass fractions during the advection step. The proposed modification is appropriate for any difference scheme written in conservation form. Unlike other commonly used methods it does not violate the conservative character of the advection method. A new steepening mechanism, which is based on modification of interpolation profiles, is used to reduce numerical diffusion across composition discontinuities. Additional procedures are described, which are necessary to enforce monotonicity. Several numerical experiments are presented which demonstrate the capability of our Consistent Multi-fluid Advection (CMA) method in case of smooth and discontinuous distributions of fluid phases and under different hydrodynamic conditions. It is shown that due to the reduced diffusivity of the proposed scheme the abundance of some heavy elements obtained from hydrodynamic simulations of type II supernova explosions can change by a factor of a few in the most extreme cases.

Key words: hydrodynamics – nuclear reactions, nucleosynthesis, abundances – methods: numerical – supernovae: general

1. Introduction

One of the most important factors determining the quality of a numerical algorithm is its robustness. In the simplest case it can be regarded as a property of the scheme to provide the result at minimum cost once the accuracy is specified. In numerical hydrodynamics much effort has been

Send offprint requests to: T. Plewa

^{*} Present address: Nicolaus Copernicus Astronomical Center, Bartycka 18, 00716 Warsaw, Poland; e-mail: tomek@camk.edu.pl

spent during the last two decades on improving advection schemes in such a way that they do not only provide high accuracy in regions of smooth flows but also resolve flow discontinuities (shocks and contact discontinuities) with a minimum number of discrete grid zones. In the past a variety of numerical experiments were conducted to compare the overall quality of solutions obtained with the help of different advection schemes which provided an understanding of the advantages and disadvantages of already available or newly proposed algorithms (Colella & Woodward 1984, Carpenter et al. 1990, Fryxell et al. 1991, Yang & Przekwas 1992, Stone & Norman 1992, Steinmetz & Müller 1993, Kang et al. 1994).

For our numerical experiments we have used the Piecewise Parabolic Method (PPM) of Colella & Woodward 1984; hereafter CW) to study the evolution of multi-fluid flows with strong discontinuities and stiff source terms. In theoretical astrophysics the PPM method has been used to study a range of hydrodynamic phenomena like stellar collisions (Ruffert & Müller 1990, Frolov et al. 1994), evolution of supersonic jets (Balsara & Norman 1992, Basset & Woodward 1995), large-scale structure formation in cosmology (Bryan et al. 1994), interaction of stellar winds in massive close binaries (Stevens et al. 1992), and the stability of radiative shock waves (Strickland & Blondin 1995). Numerical experiments of CW and Yang & Przekwas (1992) clearly demonstrated the superiority of the PPM scheme among several modern advection schemes.

A particularly interesting and challenging astrophysical problem involving multi-fluid flow (and one of our numerical experiments; see section 3.4) is the simulation of mixing in supernova envelopes. Mixing occurs because the non-steady propagation of the shock wave formed after core collapse gives rise to Rayleigh-Taylor instabilities (for a recent review, see e.g., Müller 1998). The first (2D) simulations of mixing involving ten separate fluids were performed by Arnett et al. (1989). They computed the propagation of the supernova shock wave, which was artificially created by a “point” explosion, through the envelope of a realistic stellar model. Better resolved and more detailed simulations were later performed by Fryxell et al. (1991) and Müller et al. (1991). They identified the

Rayleigh-Taylor unstable regions as being associated with discontinuities in the chemical composition in the envelope of the progenitor star. The simulations were performed with the PPM-based hydrodynamic code PROMETHEUS, which keeps track of different nuclear species by solving a set of additional continuity equations (see Fryxell et al. 1989).

In the case of single-fluid advection the problem of diffusion across contact discontinuities plays a crucial role and provides a simple test case for studying mixing between different fluids in numerical simulations. In multi-fluid flows both chemical and contact discontinuities may be present. Although, as we shall see later, there exist important differences between both kinds of discontinuities, we nevertheless can profit from our experience of modeling contact discontinuities when dealing with composition discontinuities. In this context we point out that Fryxell et al. (1989) demonstrated that the advection of a contact discontinuity is simulated better with a PPM scheme than with any other scheme they considered in their study.

Mixing of different fluids cannot be ignored if the chemical composition plays an important role in the hydrodynamic evolution. For example, in case of a realistic equation of state the total gas pressure is calculated as the sum of partial pressures exerted by each kind of species. More complex physical processes, emission from an optically thin medium (radiative cooling) or absorption of radiation, are strongly sensitive to changes in chemical composition, especially to changes in the heavy element abundances. Last but not least, the process of nuclear burning, to which we will pay special attention later in this paper, directly depends on the amount and type of nuclear fuel. In this particular case, mixing of different nuclear species due to numerical diffusion can substantially affect the final chemical composition or even the overall dynamics of the flow (for a recent review, see e.g., Müller 1998).

The paper is organized as follows. In Sect. 2 we briefly describe the basic components of the PPM scheme and some specific features implemented into the PROMETHEUS version used in our numerical experiments. We then give a detailed description of the new consistent multi-fluid advection method. In section 3 we present the results of our test simulations. A discussion of the results is contained in Sect. 4.

2. Numerical method

In what follows, we consider only the *Direct Eulerian* formulation of the PPM scheme as implemented in the PROMETHEUS code (Fryxell et al. 1989). Most of the presented results are valid for and can efficiently be implemented in codes based on the *Lagrangian with remap* approach, too. Both versions of the PPM method belong to the class of shock-capturing methods which are characterized by high-order spatial and temporal accuracy. In

such schemes flow discontinuities are treated as solutions to the hydrodynamic equations (Riemann problem) and are represented by sharp (1 to 2 zones wide) and oscillation free profiles of hydrodynamic variables. There is no need for adding large amounts of artificial viscosity for shocks to obtain correct post-shock states. PROMETHEUS uses a Strang-type directional splitting (Strang 1968) for simulation of multidimensional flows.

For given initial data and boundary conditions each hydrodynamic step of the PPM scheme begins with construction of the interpolants approximating the distribution of flow variables inside each grid zone. The initial parabolic profiles are subsequently modified according to local flow conditions: density profiles are made steeper near contact discontinuities and the distributions of all variables are somewhat flattened near shocks in order to reduce high-frequency post-shock oscillations. Afterwards, monotonicity constraints are imposed on the interpolation profiles to avoid unphysical solutions. The monotonized profiles are used to calculate initial data for the Riemann problem at each zone interface by averaging the monotonized parabolae over the domain of dependence of the zone interface. The left and right states at the interface obtained in this way define the input data for the nonlinear Riemann problem, which is solved iteratively. The solution of the Riemann problem provides average hydrodynamic state variables at the zone interface, which are used to compute the fluxes for the advection step, whereby the hydrodynamic variables are advanced to the new time level.

For simulations of mixing in supernova explosions the basic PPM algorithm was modified to allow for advection of several nuclear species. The hydrodynamic state vector was extended by adding mass fractions for each of the species as were the left and right states used as input for the Riemann problem. The effective states at zone interfaces are obtained by averaging the mass fraction profiles over a properly chosen domain of dependence for the zone interface. The interpolation step for the mass fractions also includes steepening and flattening procedures followed by a monotonization step. The mass fractions do not enter the Riemann problem. They are treated as passive scalars and are advected with the flow depending on the upwind state as determined by the average velocity obtained from the solution of the Riemann problem.

PROMETHEUS includes the handling of a general equation of state using the approach of Colella & Glaz (1985). Gravitational forces are included in the calculation of the effective states entering the Riemann problem and by a separate acceleration step at the end of each hydrodynamic sweep. Operator splitting is also used to couple nuclear burning and hydrodynamics. The nuclear reaction network is solved using a multidimensional Newton iteration (Müller 1986). A more detailed description of the implementation of PROMETHEUS can be found in Fryxell et al. (1989) and Müller (1998).

2.1. Multi-fluid advection

We consider the one-dimensional initial-boundary value problem

$$\partial_t \mathbf{U} + \partial_x \mathbf{F}(\mathbf{U}) = \mathbf{G},$$

with boundary data $\mathbf{U}(x = x_L, t)$ and $\mathbf{U}(x = x_R, t)$, where \mathbf{F} , \mathbf{U} and \mathbf{G} are the flux vector, the state vector and the vector of source terms, respectively. In case of the Euler equations for multi-fluid ideal hydrodynamics the state vector is

$$\mathbf{U} = \mathbf{U}(x, t) = \begin{pmatrix} \rho \\ \rho u \\ \rho E \\ \rho X_n \end{pmatrix}, \quad \mathbf{F}(\mathbf{U}) = \begin{pmatrix} \rho u \\ \rho u^2 + p \\ (\rho E + p)u \\ \rho X_n u \end{pmatrix},$$

where ρ , u , $E = e + u^2/2$, e , p , X_n and ρX_n are the total gas density, the velocity, the specific total energy, the specific internal energy, the pressure and the mass fraction and the partial density of the n -th fluid, respectively. The closure relation for the above system is provided by the equation of state, $p = p(\rho, e, \mathbf{X})$, where \mathbf{X} is the vector of mass fractions.

Let the number of different fluid phases be N_X and the mass fraction of the n -th fluid inside zone i be $X_{i,n}$. Then the following relation must hold for $t \geq t_0$,

$$\sum_{n=1}^{N_X} X_{i,n} = 1. \quad (1)$$

2.2. FMA method

As it has been observed first by Fryxell et al. (1989) using PROMETHEUS and by Larroutuou (1991), the nonlinear character of higher-order Godunov-type schemes is the primary reason for the violation of (1). During a simulation it is not guaranteed that in such schemes the sum of the mass fractions inside each zone remains equal to unity even if both the underlying advection scheme is conservative and the total mass of each fluid (summed over the whole grid) remains constant to within machine accuracy (see also Müller 1998).

This failure of high-order schemes can be understood when one realizes that interpolation profiles are constructed independently for each mass fraction. Thus their sum can take an arbitrary value. We notice that this problem has a predominantly local character: (i) it is most important in regions where changes in composition are substantial, and (ii) condition (1) can be violated for any subvolume of a zone (e.g. for the zone of dependence).

In practice, condition (1) is usually enforced by applying a simple renormalization of the mass fractions after each step. This procedure, however, not only lacks any formal justification but it also leads to large systematic errors in the mass fractions of the least abundant species. It also violates the conservative character of the scheme.

One possible solution to this problem is to modify the interpolation step in such a way that deviations of the sum of the mass fractions from unity will remain small inside each zone. According to the procedure proposed by Fryxell et al. (1989), which we will refer to as FMA, this can be obtained by calculating the sum of the mass fractions at the zone interface and to flatten the interpolation profiles for that zone totally, if

$$\Delta_\Sigma^\# = \left| \sum_{i=1}^{N_X} \mathbf{X}_i^\# - 1 \right| > \varepsilon_\Sigma,$$

with some predefined threshold value ε_Σ . Here, and in what follows, we take expressions involving $\#$ to mean $\#$ equal to either $+$ or $-$, where $+$ and $-$ refer to the right and left interface of the i -th zone, respectively.

In their original calculations Fryxell et al. (1989) used PROMETHEUS supplemented with FMA (with $\varepsilon_\Sigma = 10^{-7}$, while a less restrictive value of $\varepsilon_\Sigma = 10^{-3}$ seems to be acceptable for most applications). Although FMA acts only locally, in the long term it affects large regions of the grid due to its high diffusivity which effectively reduces the spatial accuracy of advection of species to first order. Consequently, one has to expect a large amount of mixing of fluids especially near composition interfaces.

2.3. CMA method

The Consistent Multi-fluid Advection (CMA) method retains the high accuracy of the PPM advection scheme for mass fractions with constraint (1) being accurately fulfilled, while any excessive flattening of interpolation profiles (as seen in case of FMA) is avoided.

The advection step can be written as,

$$\sum_{i=1}^N \rho_i \mathbf{X}_i(t + \Delta t) \Delta V_i = \sum_{i=1}^N \rho_i \mathbf{X}_i(t) \Delta V_i - \Delta t \sum_{i=1}^N (A_i^+ \mathbf{F}_i^+ - A_i^- \mathbf{F}_i^-) \quad (2)$$

where $\mathbf{F}_i^\#$ (with $\# \in \{+, -\}$) is the numerical flux vector across the zone interface of zone i which obeys the relation $\mathbf{F}_i^- = \mathbf{F}_{i-1}^+$ in any conservative scheme. $A_i^\#$ is the area of the zone interface, ΔV_i is the zone volume and Δt the size of the time step.

Since the PPM scheme is conservative, the following condition holds for each component of $\rho \mathbf{X}$ separately:

$$\sum_{i=1}^N \rho_i X_{i,n}(t) \Delta V_i = \text{const.} \quad (3)$$

By comparing (2) and (3) one obtains

$$\sum_{i=1}^N (A_i^+ \mathbf{F}_i^+ - A_i^- \mathbf{F}_i^-) = \mathbf{0}. \quad (4)$$

We seek for a set of numerical fluxes, $\mathcal{F}_i^\#$, which satisfy conditions (1) and (4) simultaneously. In general, the total mass flux at a zone interface, $\rho_i^\# u_i^\#$, computed from the sum of the mass fluxes of individual species is not necessarily equal to the total mass flux computed with the (total) mass density $\rho_i^\#$:

$$\sum_{n=1}^{N_X} F_{i,n}^\# = \sum_{n=1}^{N_X} \rho_i^\# u_i^\# X_{i,n}^\# \neq \rho_i^\# u_i^\#. \quad (5)$$

This inconsistency is the reason why any higher-order Godunov-type advection scheme in which the interpolation step for the mass fractions (or partial densities) is not appropriately constrained will violate condition (1). The inconsistency can be avoided when scaling the original partial mass fluxes $F_{i,n}^\#$ in such a way that their sum is exactly equal to the total mass flux.

We request the modified partial mass fluxes of zone i , $\mathcal{F}_{i,n}^\#$ (which depend on the modified mass fractions at the interface $\mathcal{X}_{i,n}^\#$) to be consistent with the advection of the total mass, i.e.

$$\sum_{n=1}^{N_X} \mathcal{F}_{i,n}^\# \equiv \sum_{n=1}^{N_X} \rho_i^\# u_i^\# \mathcal{X}_{i,n}^\# = \rho_i^\# u_i^\#. \quad (6)$$

Hence, we modify the original partial mass flux vector using the simple scaling operation

$$\mathcal{F}_i^\# = \varphi_i^\# \mathbf{F}_i^\#, \quad (7)$$

in such a way that it becomes consistent with the continuity equation:

$$\varphi_i^\# \sum_{n=1}^{N_X} \rho_i^\# u_i^\# X_{i,n}^\# = \rho_i^\# u_i^\#. \quad (8)$$

Comparing (6) with (8) one obtains

$$\varphi_i^\# \sum_{n=1}^{N_X} X_{i,n}^\# = \sum_{n=1}^{N_X} \mathcal{X}_{i,n}^\#, \quad (9)$$

i.e. the normalization constant, $\varphi_i^\#$, can be written in terms of the (unknown) modified mass fractions, $\mathcal{X}_{i,n}^\#$, as

$$\varphi_i^\# = \frac{\sum_{n=1}^{N_X} \mathcal{X}_{i,n}^\#}{\sum_{n=1}^{N_X} X_{i,n}^\#}. \quad (10)$$

Since the modified mass fractions are consistent with advection of the total mass by definition (6), their sum is equal to unity, i.e.

$$\varphi_i^\# = \frac{1}{\sum_{n=1}^{N_X} X_{i,n}^\#}. \quad (11)$$

In practice it is not necessary to explicitly compute the modified partial mass fluxes (7), but instead one simply

has to scale the original mass fractions $X_{i,n}^\#$ according to (9), i.e.

$$\mathcal{X}_{i,n}^\# = \varphi_i^\# X_{i,n}^\#. \quad (12)$$

The CMA method does not require any modification of the interpolation step of the advection scheme. Furthermore, it does not destroy the conservative character of the scheme (4) since the advection step (2) is invariant with respect to flux scaling. Hence, scaling the average mass fractions (12) obtained from the solution of the local Riemann problem by $\varphi_i^\#$ defined in Eq. (11) is sufficient to satisfy both (1) and (2).

In passing we note that instead of scaling the partial mass fluxes one could, in principle, appropriately adjust the total mass flux, too (which is equivalent to computing the total mass flux as the sum of the partial mass fluxes). Although numerical experiments (not presented here) demonstrate that this method produces results of comparable quality to the CMA method, we prefer to use the latter because it preserves the original role of the total gas density in the PPM method. Finally, one could discard the continuity equation for the total density and use instead the partial densities as the primary variables to calculate the total density whenever needed. We found this method to give results of overall very poor quality, and being much more diffusive near contact and composition discontinuities.

Modification (12) implemented in the original PPM advection allows us to abandon the FMA scheme, and to retain the high accuracy of the PPM method. We will refer to this algorithm as sCMA. There are, however, still some problems left to be solved. In what follows, we focus on the problem of numerical diffusion across composition interfaces, and in these cases when the nonlinearity of the advection scheme becomes too strong to preserve the monotonicity of the scheme. This will complete the description of all of the elements constituting the CMA method.

FMA uses a contact steepening mechanism which in PPM is used to limit diffusion across contact discontinuities only. Removing FMA and using the full capabilities of the PPM interpolation algorithm for mass fractions, however, revealed a severe problem. Overshooting occurred near composition interfaces for the most abundant species. This, in turn, caused the least abundant species to be evacuated out of the critical region. Clearly, in its original version the PPM contact discontinuity detection algorithm cannot be directly used to steepen distributions of mass fractions. Some additional criteria have to be used to identify composition interfaces which need to be steepened and some mechanism has to be devised which limits overshooting. We point out that in most cases the FMA method effectively prevents any steepening of mass fractions profiles, since once any of the fluid distributions has been steepened, it likely activated the FMA flattening procedure.

Since we do not expect the geometrical properties of composition interfaces to be substantially different from that of contact discontinuities, most of the original steepening algorithm can be safely used without modification for detecting large gradients in the fluid's composition. It is very unlikely to find some additional constraint similar to that originally proposed for detection of contact discontinuities (CW, Eq. 3.2) in order to make the scheme more selective. Therefore, we will only consider local properties of composition profiles. One possibility is to associate composition interfaces with rapid changes in fluid composition. For this purpose we define a steepness measure for mass fraction profiles

$$\alpha_{i,n} = \frac{X_{i+1,n} - X_{i-1,n}}{X_{i+2,n} - X_{i-2,n}}.$$

Additional steepening is applied if $\alpha_{i,n}$ is larger than a fixed value α_X . Since $\alpha_{i,n}$ has a similar meaning as the parameter ω used in PPM for calculation of the flattening coefficients (CW, Eq. A8), we set $\alpha_X = 0.75$. To prevent the steepening of relatively small composition jumps the following criterion has to be satisfied, too:

$$|X_{i+1,n} - X_{i-1,n}| - \varepsilon_x \min(X_{i+1,n} - X_{i-1,n}) > 0.$$

We use $\varepsilon_x = 0.01$. Furthermore, we do not steepen composition profiles near extrema. If the zone is located next to an extremum for which the following criteria has to be fulfilled

$$(X_{i+2,n} - X_{i+1,n})(X_{i-1,n} - X_{i-2,n}) \leq 0,$$

the steepening coefficient is set to zero. Finally, we do not steepen abundance profiles inside contact discontinuities, because this gives rise to enhanced overshooting of the partial densities, $\rho_i X_{i,n}$. After steepening we flatten and monotonize the mass fraction profiles in the same way as in PPM.

As a remedy for the overshooting near composition discontinuities, we introduce two additional modifications. Local extrema of the mass fraction distributions are identified by the criterion

$$(X_{i+1,n} - X_{i,n})(X_{i,n} - X_{i-1,n}) < 0.$$

If the criterion is fulfilled in a zone i , the interpolation profiles are flattened by an additional (constant) amount in the two zones next to it ($i \pm 1$):

$$X_{i \pm 1,n}^{\#} = w X_{i \pm 1,n} + (1 - w) X_{i \pm 1,n}^{\#}. \quad (13)$$

We use $w = 0.5$.

The second modification is somewhat more complex. For each zone we calculate two sums

$$S_i^{\#, \sigma} = \sum_{n=1}^{N_x} \max \left(0, \sigma (X_{i,n}^{\#} - X_{i,n}) \right), \quad \sigma \in \{+, -\}, \quad (14)$$

at both zone interfaces ($\# \in \{+, -\}$), which give the total positive $S_i^{\#, +}$ and negative $S_i^{\#, -}$ deviation between the

values of the mass fractions at the respective zone interface $X_{i,n}^{\#}$ and the values of the zone averaged mass fractions $X_{i,n}$.

We then correct the interface values of the mass fractions according to (13). However, instead of the constant flattening coefficient w , we use a variable coefficient $w_{i,n}^{\#}$, which depends on the positive ($S_i^{\#, +}$) and negative ($S_i^{\#, -}$) deviations defined in (14):

$$w_{i,n}^{\#} = s_{i,n}^{\#} \max \left(0, \min \left(1, \beta \frac{\Delta_{i,max}^{\#} - \Delta_{i,min}^{\#}}{\Delta_{i,min}^{\#}} \right) \right), \quad (15)$$

where

$$\Delta_{i,min}^{\#} = \min(S_i^{\#, +}, S_i^{\#, -}),$$

$$\Delta_{i,max}^{\#} = \max(S_i^{\#, +}, S_i^{\#, -}),$$

and

$$s_{i,n}^{\#} = 0.5 \left| \operatorname{sign}(X_{i,n}^+ - X_{i,n}^-) \# \operatorname{sign}(S_i^{\#, +} - S_i^{\#, -}) \right|,$$

with $\beta = 0.25$.

The reasoning behind this procedure is based on the observation that any variation in the distribution of one fluid component should be compensated by an appropriate variation of the distribution of at least one other component. Here, we define two separate groups of fluid components which show deviations (from the zone average) of the same sign at the zone interface. Once the sums of the negative (S^-) and the positive (S^+) deviations are obtained, we try to limit their relative difference. Note that the FMA flattening criterion is based on the absolute value of the deviation of the sum $S^{\#, +} + S^{\#, -}$ from unity.

In the CMA method the amount of additional flattening is not constant but smoothly increases with the relative difference between the two deviations. Maximum flattening is applied if the relative difference between the two deviations exceeds $1/\beta$, while no additional flattening is introduced for $\beta = 0$. Hence, when $\beta > 0$, the interpolation profiles for that group of species which shows the largest absolute deviation are modified using the same flattening coefficient for all species. This reduces the deviation and brings it closer to that of the other group of species.

In this way we introduce a finite amount of coupling between the interpolation profiles of two distinct groups of fluid components rather than trying to adjust the distributions of fluid components individually. Since the additional flattening procedure has a strictly dissipative character and relies on flattening of interpolation profiles, it is very unlikely that it causes unphysical solutions.

Finally, we mention that the just described procedure could also be used to guarantee consistency between the total mass flux and the sum of the partial mass fluxes. Hence, it could be applied both in the interpolation and the advection step.

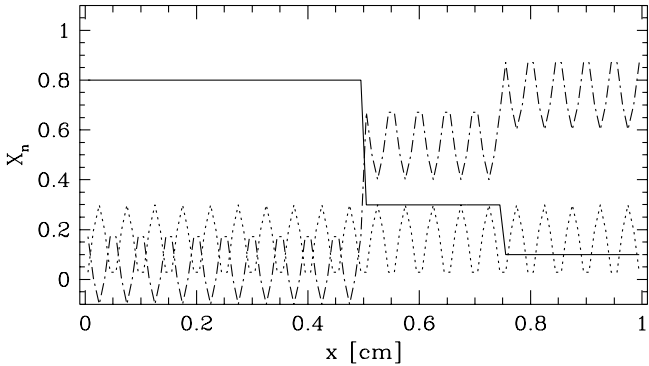


Fig. 1. Initial distribution of fluid phases in Sod's shock tube problem: X_1 – solid line; X_2 – dashed line; X_3 – dash-dotted line.

3. Results

We have performed several numerical tests to illustrate problems arising in multi-fluid flows (when simulated with PROMETHEUS) and to demonstrate the capability of the CMA method.

3.1. Shock tube

The first problem is the shock tube test problem originally proposed by Sod (1978). We have modified this problem to include three passively advected fluids. The initial state for this problem (Fig. 1) is,

$$U(0 \leq x \leq 0.5, t = 0) = \begin{pmatrix} \rho \\ u \\ p \end{pmatrix} = \begin{pmatrix} 1 \\ 0 \\ 1 \end{pmatrix},$$

and

$$U(0.5 < x \leq 1.0, t = 0) = \begin{pmatrix} \rho \\ u \\ p \end{pmatrix} = \begin{pmatrix} 0.125 \\ 0 \\ 0.1 \end{pmatrix},$$

with a discontinuous distribution of X_1 ,

$$X_1(x, t = 0) = \begin{cases} 0.8, & 0 \leq x \leq 0.5, \\ 0.3, & 0.5 < x \leq 0.75, \\ 0.1, & \text{otherwise,} \end{cases}$$

and oscillating mass fractions of the two other fluids,

$$\begin{aligned} X_2 &= 0.3 \sin^2(20\pi x), \\ X_3 &= 1 - X_2 - X_1. \end{aligned}$$

The simulations have been performed with an ideal gas equation of state with $\gamma = 1.4$, and an equidistant grid of 100 zones. Reflecting boundary conditions were imposed on both ends ($x = 0$ and $x = 1$) of the computational domain.

We obtained three sets of results for different code configurations: original PPM code (Fig. 2, top row), PPM with FMA (middle section, $\varepsilon_\Sigma = 10^{-3}$), and PPM with

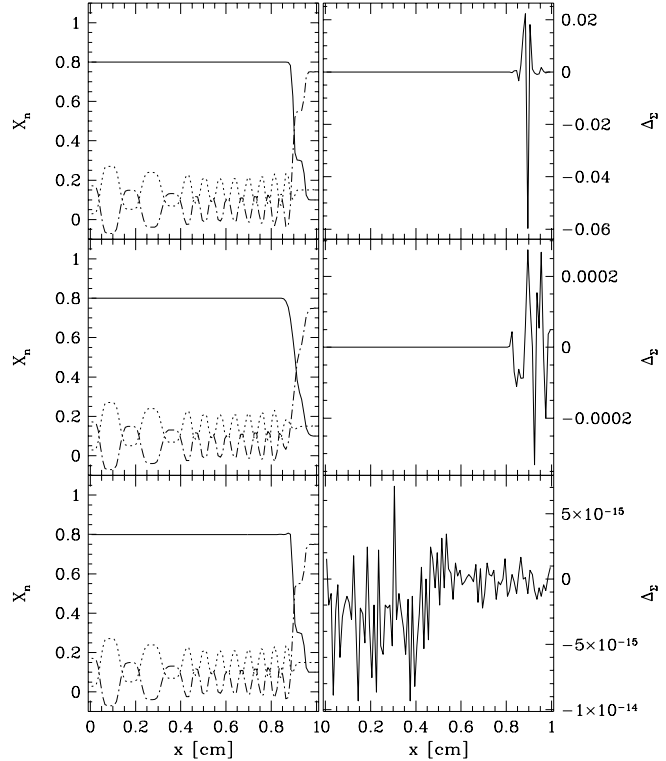


Fig. 2. Distributions of fluid phases (left) and deviations of the sum of mass fractions from unity (right) in Sod's shock tube problem at time $t = 1$ for three different runs: original PPM code (top), PPM with FMA (middle), and PPM with sCMA (bottom). X_1 – solid line; X_2 – dashed line; X_3 – dash-dotted line.

CMA (bottom part) but with no special modifications of the interpolation algorithm included (sCMA). The left panels of Fig. 2 show the distributions of the fluids (X_1 – solid line, X_2 – dashed, X_3 – dash-dotted), while the right panels give the deviations of the sum of the mass fractions from unity, Δ_Σ (see Eq. (2.2)).

The comparison of mass fraction profiles of different models at $t = 1$ (Fig. 2) shows a good agreement for $x \lesssim 0.85$ except for some small amount of clipping near the extrema of X_2 and X_3 . However, we find large differences near the jump in X_1 at $x \approx 0.87$. The amplitude of the sinusoidal variation of X_2 and X_3 is significantly reduced in case of FMA, and the initial discontinuities in X_1 are strongly smeared. The original PPM scheme and the sCMA scheme are much less diffusive. Both jumps in X_1 are clearly separated and the profiles of X_2 and X_3 do smoothly vary near $x \approx 0.87$.

The differences are even larger near the right boundary of the computational domain (Fig. 2). PPM strongly violates condition (1). $\sum X_i$ deviates from unity by up to 6% (where X_1 is discontinuous). The errors are much smaller for FMA the deviations only being of the order of 10^{-4} which is close to the chosen value of ε_Δ . However,

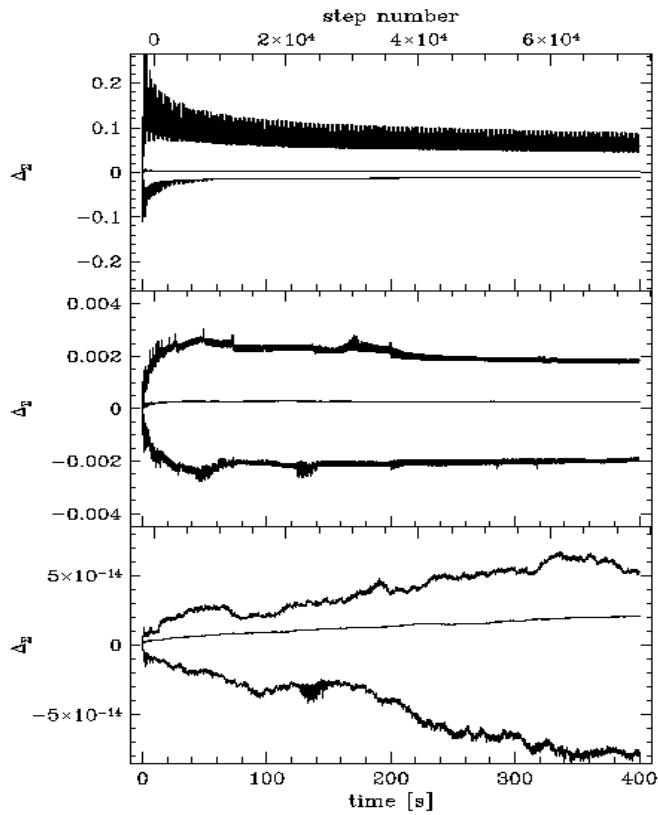


Fig. 3. Long-term behaviour of mean and extreme deviations from condition (1) in Sod's shock tube problem. Top: original PPM; middle: FMA; bottom: sCMA.

as already noted above, the smaller error is bought at the cost of a degraded resolution. The sCMA method gave the best result. It does not only advect the fluids with high accuracy, but it is also able to keep $\sum X_i = 1$ at the level of machine accuracy. The only imperfection one notices is some overshoot in the distribution of X_1 just to the left of the larger discontinuity signaling the first sign of a need for additional modifications of the interpolation scheme of the mass fractions (especially near composition interfaces).

To observe the long term behaviour of the three schemes we continued our simulations up to $t = 400$ (more than 75 000 steps with a Courant number of 0.8). Figure 3 shows the evolution of the maximum negative and positive deviations from condition (1) recorded for each time step together with the mean absolute value of the deviation from unity averaged over all zones. The results for the original PPM method (top panel in Fig. 3) indicate large variations (in excess of 20%) which would certainly destroy any solution sensitive to chemical composition. When using FMA we observe a rapid rise of the maximum error which levels off after slightly exceeding $2 \varepsilon_\Delta$. The results obtained with sCMA show a slow growth of the maximum and minimum deviations, which seem to saturate at later times.

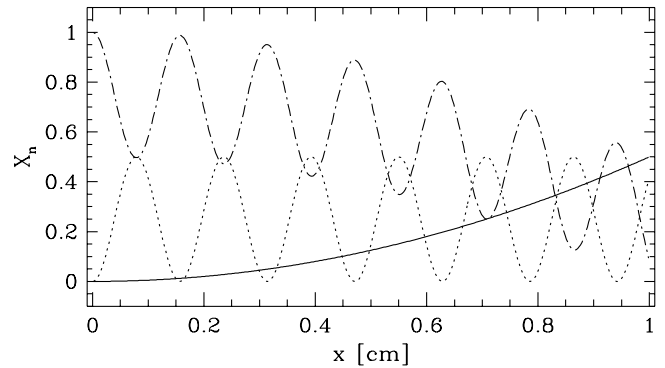


Fig. 4. Initial distributions of fluid phases in the interacting blast waves test problem: X_1 – solid line; X_2 – dashed line; X_3 – dash-dotted line.

3.2. Two interacting blast waves

This test problem was originally proposed by Woodward (1982). It gained much of its popularity later when being used by Woodward & Colella (1984) in their study of various advection schemes in case of flows with strong shocks. In this problem the initial state consists of a low-pressure region located in the central part of the grid,

$$U(0.1 < x < 0.9, t = 0) = \begin{pmatrix} \rho \\ u \\ p \end{pmatrix} = \begin{pmatrix} 1 \\ 0 \\ 0.01 \end{pmatrix},$$

which is bounded by two regions of (different) high pressure

$$U(0 \leq x \leq 0.1, t = 0) = \begin{pmatrix} \rho \\ u \\ p \end{pmatrix} = \begin{pmatrix} 1 \\ 0 \\ 1000 \end{pmatrix},$$

and

$$U(0.9 \leq x \leq 1, t = 0) = \begin{pmatrix} \rho \\ u \\ p \end{pmatrix} = \begin{pmatrix} 1 \\ 0 \\ 100 \end{pmatrix}.$$

For our test runs we used three passively advected fluids with mass fractions that are initially varying smoothly across the entire grid (Fig. 4)

$$\begin{aligned} X_1 &= 0.5x^2, \\ X_2 &= 0.5 \sin^2(20x), \\ X_3 &= 1 - X_2 - X_3. \end{aligned}$$

Again, we use an ideal gas equation of state with $\gamma = 1.4$. The grid consists of 400 equidistant zones. Reflecting conditions are imposed at both grid boundaries.

The results of our simulations at $t = 0.038$ are shown in Fig. 5.

Since this time the initial distributions of the fluids are smooth we do not expect to see any discontinuities in the distributions of the mass fractions at later times.

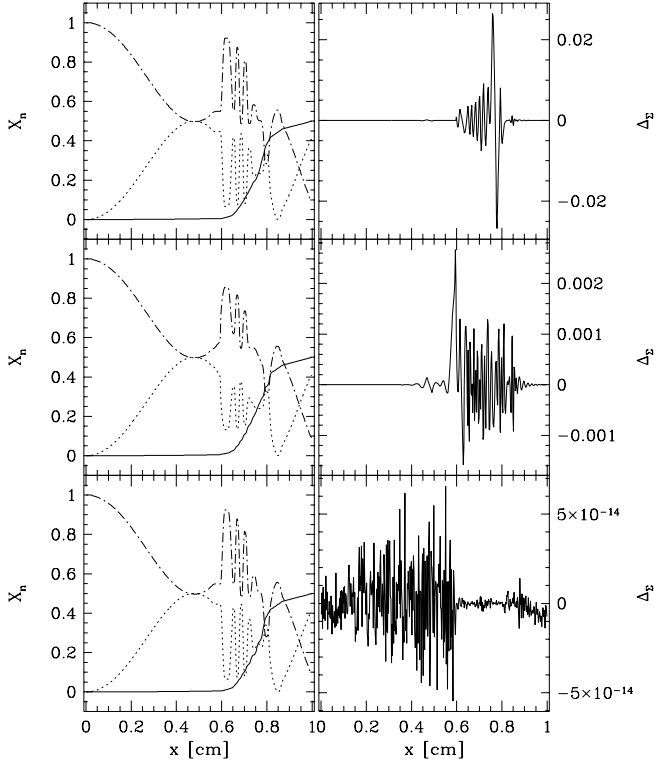


Fig. 5. Distributions of fluid phases (left) and deviations of the sum of mass fractions from unity (right) in the interacting blast wave problem at time $t = 0.038$ for three different runs: original PPM code (top), PPM with FMA (middle), and PPM with sCMA (bottom). X_1 – solid line; X_2 – dashed line; X_3 – dash-dotted line.

However, a discontinuity is created in the X_2 and X_3 distributions at $x \approx 0.6$ when using the original PPM and the sCMA method (left column, top and bottom panel of Fig. 5, respectively). No such discontinuity is present in the FMA data (middle panel). We identify the creation of such spurious composition interfaces with the actual failure of the unmodified discontinuity detection procedure of PPM (see Section 2.3). FMA once again proves to be more diffusive than the other two schemes: high-amplitude variations of X_2 and X_3 as seen in the PPM and sCMA data for $0.6 \lesssim x \lesssim 0.8$ have markedly smaller amplitudes when calculated with FMA. Moreover, there is no trace of an extremum in X_3 at $x \approx 0.75$. In other parts of the grid all three methods produce very similar results.

As in the case of Sod's shock tube problem the condition (1) is most strongly violated when the original PPM method is used (upper left panel in Fig. 5). The maximum deviation of 2% occurs in that region where the FMA results are mostly affected by the use of an additional flattening procedure. On the other hand, FMA violates condition (1) at the level of ε_Δ with a single pronounced maximum at the spurious composition interface created in the other two schemes. The sCMA method produces the

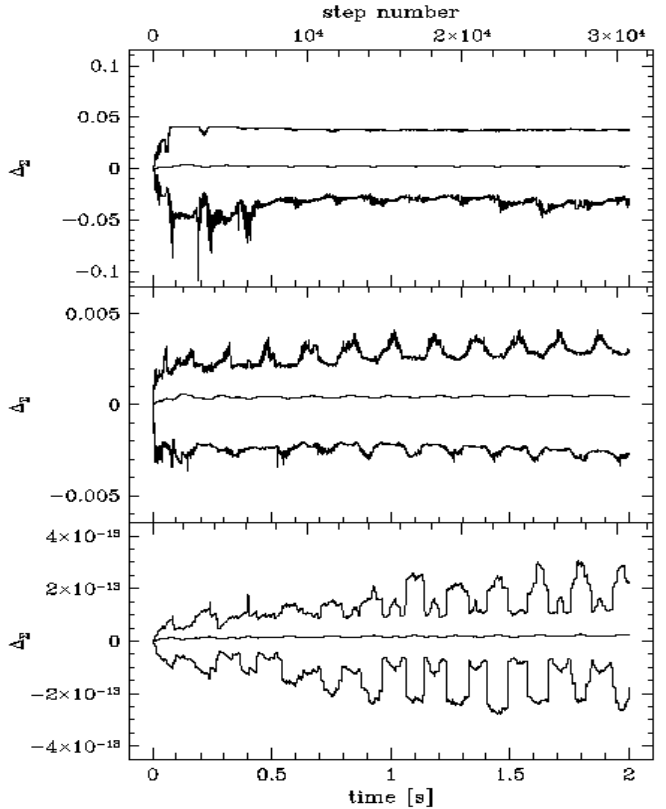


Fig. 6. Long-term behaviour of mean and extreme deviations from condition (1) in the colliding blast waves problem. Top: original PPM; middle: FMA; bottom: sCMA.

most accurate results both during the initial phases of the evolution and in the long term evolution (lower left panel in Fig. 6). The maximum deviations from (1) exceed 10% for the original PPM method and fluctuate between 2 and 3 times ε_Δ in case of FMA.

3.3. Shock-contact interaction

The initial state for this problem is,

$$U(0 \leq x \leq 0.1, t = 0) = \begin{pmatrix} \rho \\ u \\ p \end{pmatrix} = \begin{pmatrix} 1 \\ 0 \\ 1000 \end{pmatrix},$$

$$U(0.1 < x \leq 0.5, t = 0) = \begin{pmatrix} \rho \\ u \\ p \end{pmatrix} = \begin{pmatrix} 1 \\ -1 \\ 0.01 \end{pmatrix},$$

and

$$U(0.5 < x \leq 1, t = 0) = \begin{pmatrix} \rho \\ u \\ p \end{pmatrix} = \begin{pmatrix} 10^4 \\ -1 \\ 0.01 \end{pmatrix},$$

with $X_1 = 0.2$ for $x < 0.15$, $X_1 = 0.6$ for $x \geq 0.15$, and
 $X_2 = 0.3 \sin^2(30x) + 0.001$,
 $X_3 = 1 - X_1 - X_2$.

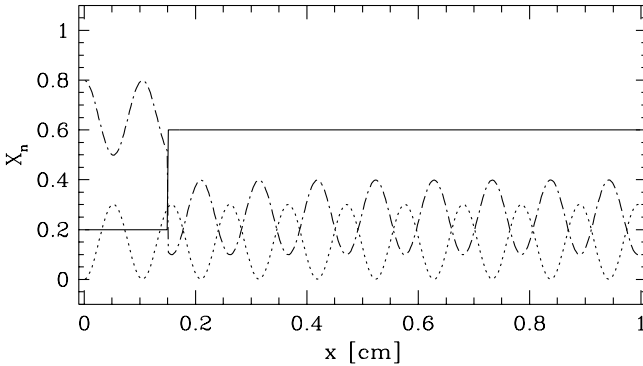


Fig. 7. Initial distributions of fluid phases for the shock-contact interaction problem: X_1 – solid line; X_2 – dashed line; X_3 – dash-dotted line.

The initial abundances with a composition interface between X_1 and X_3 at $x = 0.15$ are shown in Fig. 7. Again an ideal gas equation of state with $\gamma = 1.4$ is used. The grid contains 400 equidistant zones. The left grid boundary is reflecting, while a flow-in boundary condition is imposed at the right grid boundary. The state of the inflowing gas is equal to that of the gas located near that boundary at the initial time.

The initial conditions create a strong shock wave at $x = 0.1$ which propagates towards the left, hits the composition interface (initially located at $x = 0.15$) and then collides with the strong contact discontinuity (initially located at $x = 0.5$) that slowly moves to the left. Upon interaction a pair of shocks is generated.

Figure 8 shows the distribution of the mass fractions together with the deviations from the condition (1) at $t = 0.045$ after all strong interactions have already taken place. All three methods give comparable results in regions of pure advective flow ($x \gtrsim 0.4$). Towards the left follows a region with low-amplitude variations in the distributions of X_2 and X_3 , which is much more diffused when calculated with FMA (middle left panel in Fig. 8). The composition interface ($x \approx 0.25$) also seems to be smeared out in case of FMA, but it remains sharp in the other two cases. Finally, there is some overshoot in the distribution of X_1 which can be seen just to the right of the composition interface in the sCMA data. The interface is slightly broader when calculated with the sCMA method than with the original PPM method primarily because of the smooth rounded profile associated with the overshoot.

The analysis of deviations from condition (1) (right column in Fig. 8) confirms our conclusions from the previous tests. Original PPM produces deviations of the order of a few percent. Most of the extra diffusion used by FMA to keep deviations small occurs in the region of interaction between the shock and the contact discontinuity, and near the composition interface. It is in this region where differences in abundances between FMA and the other two codes are most apparent. The long term behaviour of the

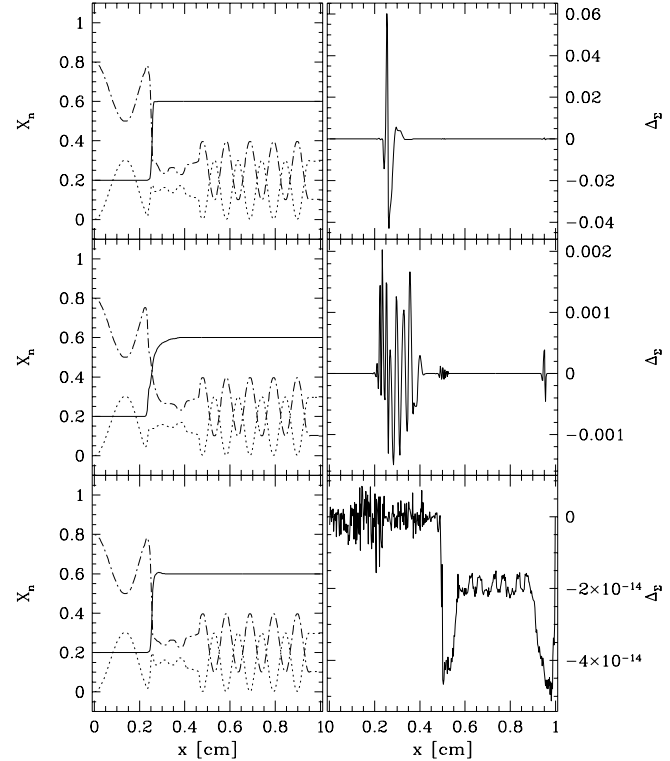


Fig. 8. Distributions of fluid phases (left) and deviations of the sum of mass fractions from unity (right) in the shock-discontinuity interaction problem at time $t = 0.045$ for three different runs: original PPM code (top), PPM with FMA (middle), and PPM with sCMA (bottom). X_1 – solid line; X_2 – dashed line; X_3 – dash-dotted line.

deviations (Fig. 9) indicates that there is no tendency for deviations to become smaller with time. Using the original version of PPM we find errors in the several percent range (up to 10%). The typical deviations for FMA are between 2 and 3 times ε_Δ . There is some systematic increase in deviations visible in case of sCMA at late times, but it does not seem to be of any importance.

3.4. Supernova explosion

For our final “numerical” example we have chosen the shock propagation during the post-bounce evolution of a core collapse supernova. We consider the very early ($t \leq 3$ s) stages of the evolution, when the just born supernova shock begins to sweep through the stellar layers just outside the iron core triggering nuclear synthesis. We will focus our attention on the role which numerical diffusion plays in the process of nuclear burning and on its impact on the final chemical composition of the thermonuclear processed material.

For these calculations we have used PROMETHEUS in a version which allowed us to consider those physical processes which play an important role during the early

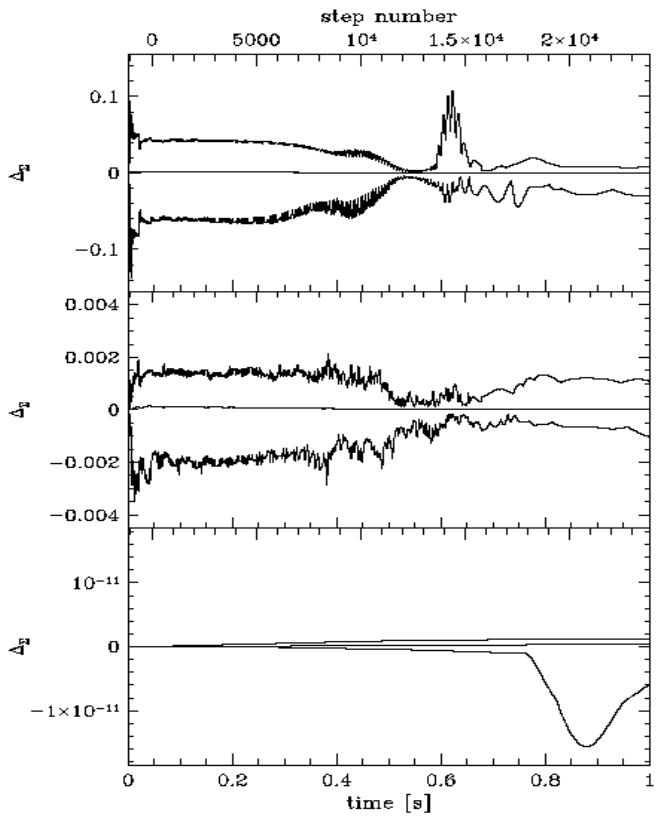


Fig. 9. Long-term behaviour of mean and extreme deviations from condition (1) in the shock-contact interaction problem. Top: original PPM; middle: FMA; bottom: sCMA.

phases of the shock propagation. The gas is assumed to be a mixture of 14 nuclei (^1H , ^4He , ^{12}C , ^{16}O , ^{20}Ne , ^{24}Mg , ^{28}Si , ^{32}S , ^{36}Ar , ^{40}Ca , ^{44}Ti , ^{48}Cr , ^{52}Fe , ^{56}Ni). An α -network with 27 reactions coupling 13 of these nuclei (all except ^1H) is used to describe nuclear burning. The approximate equation of state includes contributions from radiation, the 14 fully ionized Boltzmann gases, and positron-electron pairs (included in an approximate way). Self-gravity of the stellar envelope is taken into account as well as the gravitational attraction of a central point source which mimics the nascent neutron star ($M_{\text{ns}} \approx 1.28 M_{\odot}$).

The simulations have been performed in one spatial dimension assuming spherical symmetry. At the inner edge of the grid a reflecting boundary condition is imposed, while free outflow is allowed through the outer boundary. The inner boundary is situated at $r_{in} = 1.376 \times 10^8 \text{ cm}$ corresponding to a mass coordinate of $1.317 M_{\odot}$, which is well inside the Si shell. The computational domain, which extends out to a radius of $6.4 \times 10^9 \text{ cm}$, is covered by 1600 zones (corresponding to a resolution of 40 km) in our standard resolution run. Additional simulations with up to 12 800 zones (corresponding to a resolution of 5 km) have

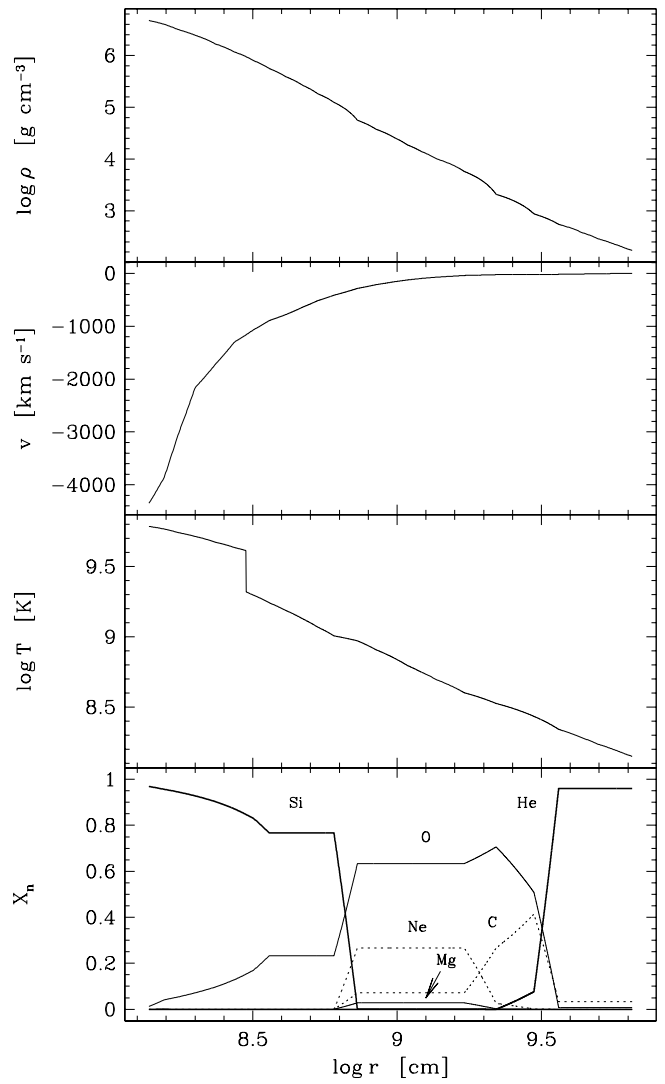


Fig. 10. Density, velocity, temperature and composition profiles for the most abundant species (from top to bottom) of the $15 M_{\odot}$ progenitor model. The high temperature region in the innermost ($r \leq 3 \times 10^8 \text{ cm}$) part of the Si shell results from the deposition of 10^{51} ergs of internal energy in order to initiate the explosion.

been performed to study the convergence behaviour of different advection schemes.

The initial model is a $15 M_{\odot}$ pre-collapse model of a blue supergiant (S. Woosley, private communication), which closely resembles a progenitor model of SN 1987A (Woosley, Pinto & Enzman 1988). The density, velocity and temperature profiles of the initial model are shown in Fig. 10.

In order to launch the supernova shock wave, we created a thermal bomb by adding $E_{\text{tb}} = 10^{51} \text{ ergs}$ in form of internal energy to the innermost ($r \leq 3 \times 10^8 \text{ cm}$) parts of the Si shell. The resulting shock wave propagates rapidly outwards heating up the stellar matter. Simultaneously

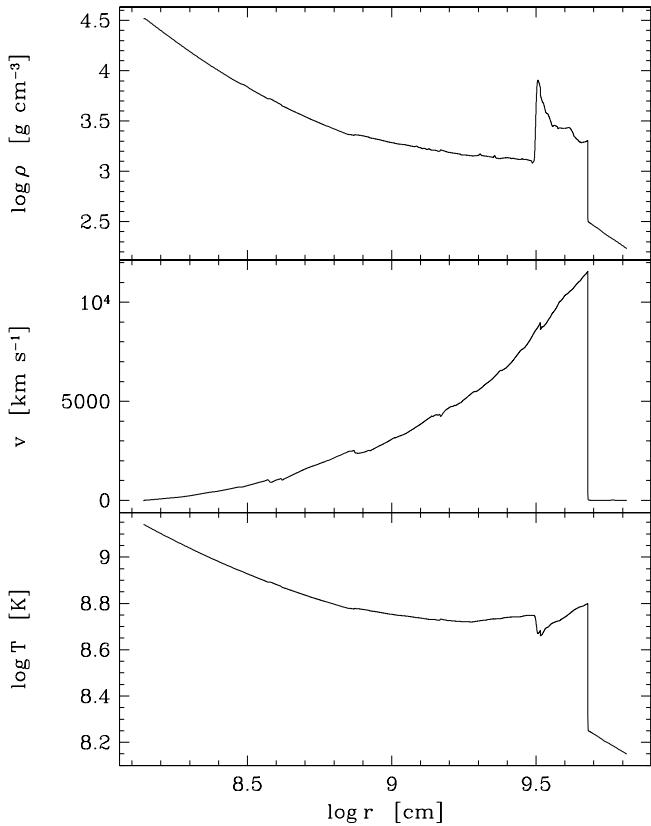


Fig. 11. Density (top), velocity (middle) and temperature (bottom) profiles of the progenitor at $t = 3$ s obtained with the CMA method and a grid resolution of $\Delta r = 10$ km. The supernova shock has reached the helium shell and hence has already passed several composition interfaces. At every interface a weak reflected shock is created, which can be recognized in the velocity profile. The large density jump near $r \approx 10^{9.5}$ cm separates shocked gas that initially formed the thermal bomb from matter in the stellar envelope.

a much weaker reverse shock propagates inwards. The temperatures and densities behind the supernova shock are sufficiently high to trigger thermonuclear burning and the production of new elements. The resulting release of nuclear energy slightly enhances the explosion energy. Whenever the outward propagating shock crosses one of the composition interfaces of the progenitor star (see Fig. 10), a weak reflected shock is created. The reflected shocks move inwards reheating the matter, which has just been processed by the supernova shock (see velocity profile in Fig. 11). A strong contact discontinuity at $r \approx 10^{9.5}$ cm corresponding to the mass coordinate $M_r \approx 1.415 M_\odot$ separates the shocked envelope gas from matter initially belonging to the thermal bomb.

Figure 12 shows the evolution of the chemical composition obtained with the FMA method at a resolution of 40 km in a narrow mass range ($\sim 0.1 M_\odot$) close to the

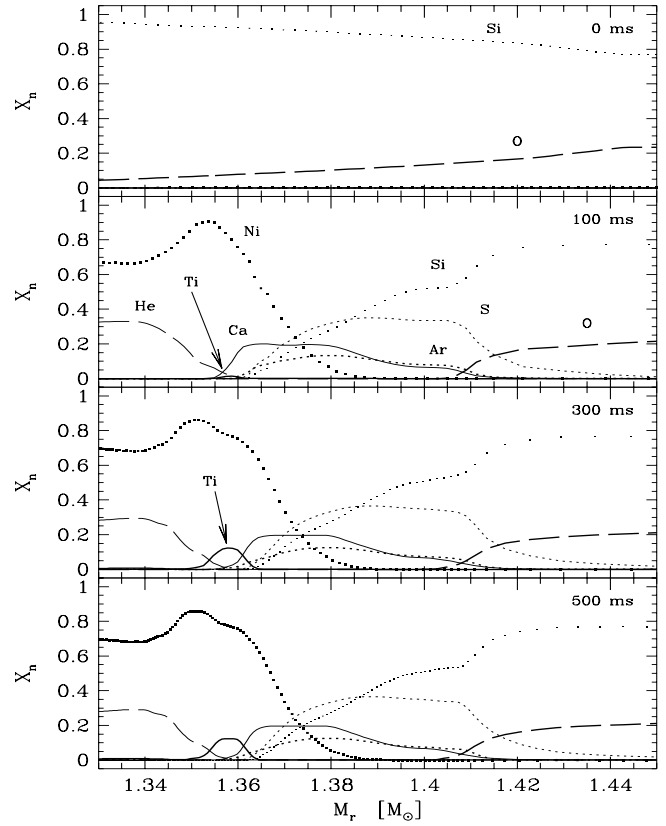


Fig. 12. Chemical composition of the ejecta obtained with the FMA method as a function of mass coordinate at $t = 0, 100, 300$, and 500 ms (from top to bottom). The grid resolution is 40 km.

outer edge of the thermal bomb. Nuclear burning is most intense very early on ($t < 100$ ms) when matter is still dense and hot. At later times the chemical composition does not change appreciably with one exception. Production of ^{44}Ti only begins around $t = 100$ ms (a barely visible bump between 1.355 and $1.36 M_\odot$) and lasts for $\simeq 300$ ms.

In many aspects the evolution is similar when calculated with the CMA method at the same grid resolution (Fig. 13). However, some important differences also exist. With the CMA method mixing between ^{16}O and other nuclear species at $M_r \approx 1.415 M_\odot$ is greatly reduced. ^{36}Ar and ^{40}Ca are clearly separated from oxygen at $t = 500$ ms. There is an indication of a ^{28}Si interface near $M_r \approx 1.41 M_\odot$. The transition region extends only over two zones (over about 5 zones in case of FMA) and is accompanied by a small amount of overshooting towards larger radii. This region is difficult to model due to the presence of the strong contact discontinuity separating the stellar envelope from the thermal bomb. Without additional flattening and monotonization of the mass fraction profiles (as described in section 2.3) the overshooting of ^{28}Si is suspiciously large. We note that overshooting of the most abundant species near composition interfaces might be a common problem for hydrodynamic codes (see, for

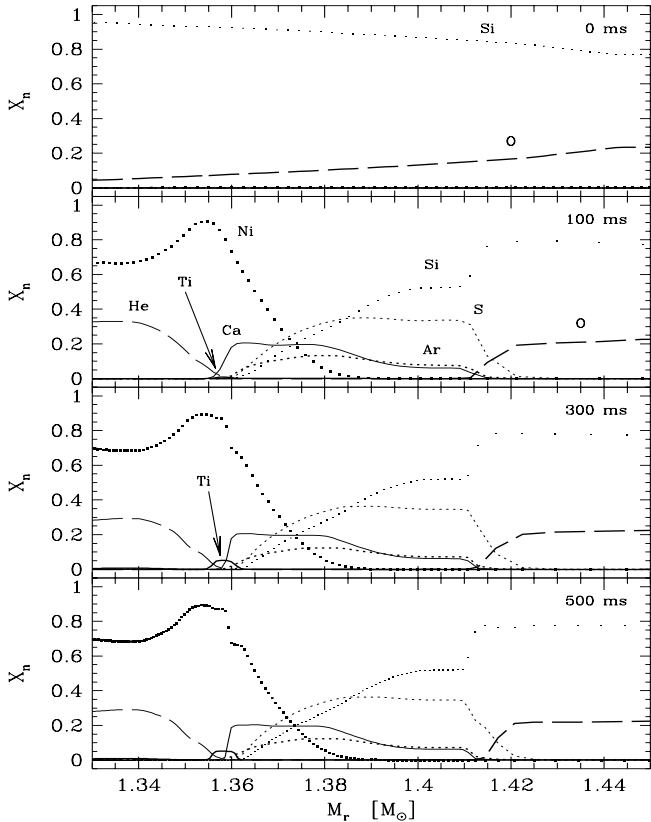


Fig. 13. Chemical composition of the ejecta obtained with the CMA method as a function of mass coordinate at $t = 0, 100, 300$, and 500 ms (from top to bottom). The grid resolution is 40 km.

example, Fig. 4 of Woosley, Pinto & Enzman 1988), and certainly deserves further investigation.

Another difference between the FMA and CMA results is the mass of ^{44}Ti produced in the simulations, which seems to be quite sensitive to the amount of numerical diffusion. Since titanium is synthesized via the reaction $^{40}\text{Ca}(\alpha, \gamma)^{44}\text{Ti}$ and since enhanced diffusion results in a smoother distribution of calcium, we computed several models where the interpolation profile for calcium was constructed assuming four different constant flattening coefficients f_{Ca} (models $f_{0.25}$, $f_{0.50}$, $f_{0.75}$ and $f_{1.00}$, respectively). An additional extreme model (CMAZ) was calculated where all mass fraction profiles are flattened completely thereby imposing a maximum amount of numerical diffusion. The results (Fig. 14) show that the amount of ^{44}Ti is smallest when using CMA ($5.0 \times 10^{-4} M_{\odot}$), that it increases linearly with f_{Ca} and that the result of FMA ($1.22 \times 10^{-3} M_{\odot}$) is recovered when the calcium profile is kept totally flat throughout the simulation (model $f_{1.00}$). In case of maximum numerical diffusion (model CMAZ) the amount of titanium ($1.69 \times 10^{-3} M_{\odot}$) is even larger and exceeds that obtained with CMA by a factor of more than three. Table 1 summarizes these results; data taken from model 15A of Woosley, Pinto & Enzman (1988) (who

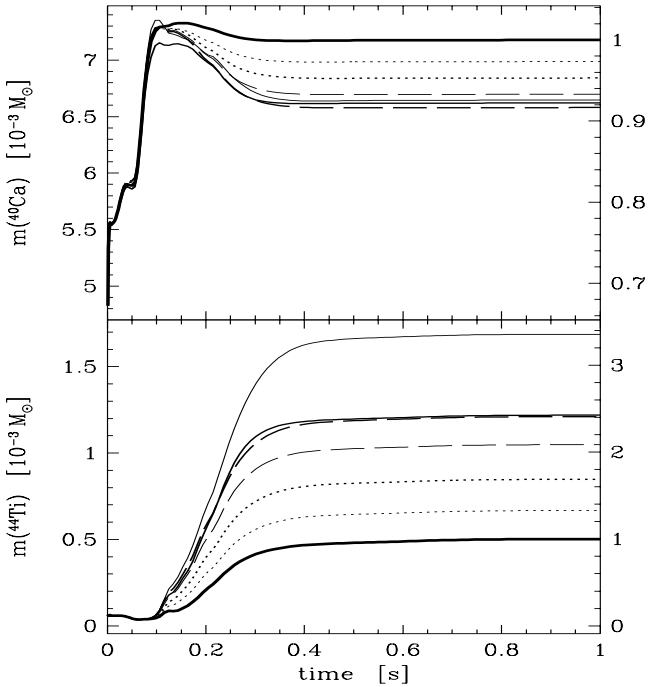


Fig. 14. Total mass of ^{40}Ca (upper part) and ^{44}Ti (lower part) as a function of time obtained with different advection schemes. Solid lines: CMAZ (thin), FMA (medium), CMA (thick). CMA results with additional flattening for ^{40}Ca are shown by dashed lines for f_{Ca} equal to 0.25 (thin), 0.50 (thick), 0.75 (long thin), and 1.00 (long thick). The scale on the right side gives the masses normalized to the respective final mass obtained with CMA.

Table 1. Total masses of ^{40}Ca and ^{44}Ti (in units of M_{\odot}) at $t = 3$ s

model	^{40}Ca	^{44}Ti
CMA	0.00718	0.00050
$f_{0.25}$	0.00699	0.00067
$f_{0.50}$	0.00684	0.00085
$f_{0.75}$	0.00670	0.00105
$f_{1.00}$	0.00658	0.00121
FMA	0.00662	0.00122
CMAZ	0.00665	0.00169
WPE ^a	0.006	0.0002

^a Model 15A of Woosley, Pinto & Enzman (1988).

used a different mechanism to initiate the explosion!) are also shown for comparison.

Figure 15 shows the composition profiles in the ejecta at $t = 3$ s for our three basic models: CMAZ (top), FMA (middle), and CMA (bottom). In CMAZ all abundances change smoothly and no particular feature can be recognized. In CMA there exist composition interfaces of ^{40}Ca ($\log r \approx 9.36$), ^{16}O and ^{32}S ($\log r \approx 9.5$), and several dis-

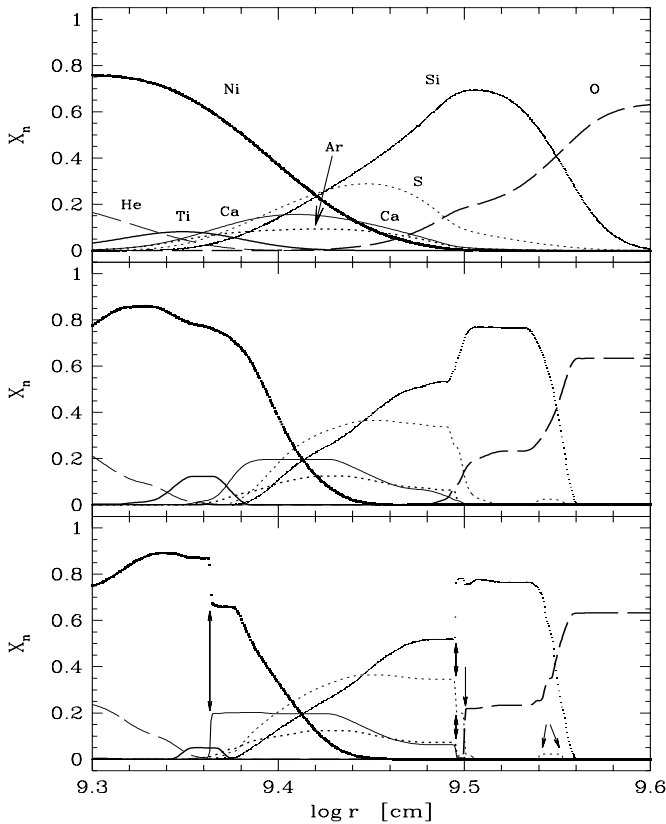


Fig. 15. Composition structure of the progenitor at $t = 3$ s: CMAZ (top), FMA (middle), CMA (bottom).

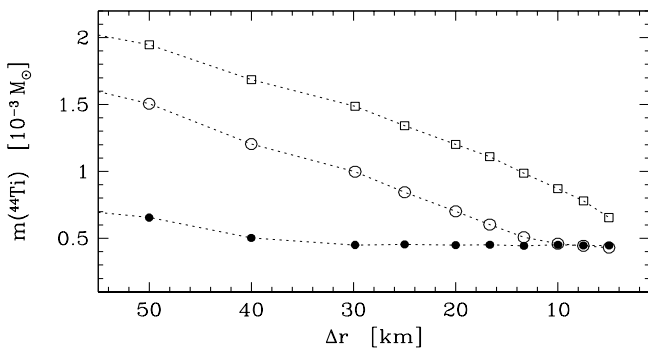


Fig. 16. Dependence of the production of ^{44}Ti on the grid resolution. The total ^{44}Ti mass is shown as a function of resolution at $t = 3$ s for models CMAZ (open squares), FMA (open circles), and CMA (full circles), respectively.

continuities (in ^{28}Si , ^{32}S , ^{36}Ar , ^{40}Ca) at $\log r \approx 9.5$. Out of these only a relatively weak discontinuity in the distribution of ^{36}Ar can be recognized in the FMA model.

Finally, we have studied the convergence properties with respect to the production of heavy elements in our three schemes. The results for ^{44}Ti (Fig. 16) indicate that with CMAZ and FMA the production of titanium decreases as the resolution is improved. More interestingly, the CMA results depend only weakly on the resolution.

This behaviour can be understood if we realize that there exists a composition interface in calcium near which titanium is formed, and that (as demonstrated by our numerical experiments; Fig. 14) the production of titanium grows with the diffusivity of the advection scheme. Once the composition interface is resolved and properly handled by the code, the final mass of titanium becomes practically independent of the spatial grid resolution.

4. Summary and conclusions

We have derived a numerical approach which guarantees that the sum of mass fractions equals unity in simulations of multi-fluid flows with higher-order Godunov-type methods. Unlike other commonly used numerical methods, the proposed scheme preserves the conservative character of the underlying advection scheme.

Modifications of the interpolation step are needed in higher-order Godunov-type methods to reduce the numerical diffusion near composition interfaces. These modifications are described together with procedures that ensure the monotonicity of the scheme.

The Consistent Multi-fluid Advection method (CMA) is proposed as a new method to accurately describe multi-fluid flows. The CMA method is implemented in the PPM-based hydrodynamic code PROMETHEUS and applied to several 1D test problems with both smooth and discontinuous composition profiles. The numerical examples involve flows with strong hydrodynamic discontinuities. They convincingly demonstrate the validity and capability of the CMA method.

It is shown that numerical diffusion near composition interfaces can change the composition of supernova ejecta by a factor of a few. The abundance of titanium is most severely affected in our test calculations. The consequences of these findings for explosive nucleosynthesis calculations should be explored in more detail.

Acknowledgements. We thank Stan Woosley for providing us with his unpublished presupernova models. We also like to thank Konstantinos Kifonidis, who provided software (reaction network) and helped with many critical and useful comments during the course of this work. TP was partly supported by grant 2.P03D.004.13 from the Polish Committee for Scientific Research. The major part of the simulations was performed on the RISC cluster of the MPA, and on the SGI Power Challenge at the Interdisciplinary Centre for Computational Modelling in Warsaw.

References

- Arnett, W.D., Fryxell, B.A., Müller, E., 1989, ApJ 341, L63
- Balsara, D.S., Norman, M.L., 1992, ApJ 393, 631
- Bassett, G.M., Woodward, P.R., 1995, ApJ 441, 582
- Bryan, G.L., Cen, R., Norman, M.L., Ostriker, J.P., Stone, J.M., 1994, ApJ 428, 405
- Carpenter, R.L. Jr., Droege, K.K., Woodward, P.R., Hane, C.E., 1990, Mon. Wea. Rev. 118, 586

Colella, P., Glaz, H.M., 1985, *J. Comput. Phys.* 59, 264

Colella, P., Woodward, P.R., 1984, *J. Comput. Phys.* 54, 174
(CW)

Frolov, V.P., Khokhlov, A.M., Novikov, I.D., Pethick, C.J., 1994, *ApJ* 432, 680

Fryxell, B.A., Müller, E., Arnett, W.D., 1989, Max-Planck-Institut für Astrophysik, Preprint 449, Garching (FMA)

Fryxell, B.A., Müller, E., Arnett, W.D., 1991, *ApJ* 367, 619

Kang, H., Ostriker, J.P., Cen, R., Ryu, D., Hernquist, L., Evrard, A.E., Bryan, G.L., Norman, M.L., 1994, *ApJ* 430, 83

Larrouture, B., 1991, *J. Comput. Phys.* 95, 59

Müller, E., 1986, *A&A* 162, 103

Müller, E., 1998, in: Computational Methods for Astrophysical Fluid Flow, 27th Saas-Fee Advanced Course Lecture Notes, eds. O. Steiner and A. Gautschy (also Max-Planck-Institut für Astrophysik, Preprint 1060, Garching)

Müller, E., Fryxell, B.A., Arnett, W.D., 1991, *A&A* 251, 505

Ruffert, M., Müller, E., 1990, *A&A* 238, 116

Sod, G.A., 1978, *J. Comput. Phys.* 27, 1

Stevens, I.R., Blondin, J.M., Pollock, A.M.T., 1992, *ApJ* 386, 265

Steinmetz, M., Müller, E., 1993, *A&A* 268, 391

Stone, J.M., Norman, M.L., 1992, *ApJS* 80, 753

Strang, G., 1968, *SIAM J. Numer. Anal.* 5, 506

Strickland, R., Blondin, J.M., 1995, *ApJ* 449, 727

Woodward, P.R., 1982, in: Parallel Computations, ed. G. Rodrigue, Academic Press, New York

Woodward, P.R., Colella, P., 1984, *J. Comput. Phys.* 54, 115

Woosley, S.E., Pinto, P.A., Enzman, L., 1988, *ApJ* 324, 466

Yang, H.Q., Przekwas, A.J., 1992, *J. Comput. Phys.* 102, 139